Journal of Advanced Ceramics
先进陶瓷
ISSN 2226-4108
CN 10-1154/TQ
清華大學出版社 Tsinghua University Press
SciOpen

J Adv Ceram 2026, **15**: 9221413

https://doi.org/10.26599/JAC.2026.9221413

Research Article

Interfacial reactions and properties of tungsten–silicon nitride composites prepared by spark plasma sintering

Yu Zhou, Wensheng Liu*, Yunzhu Ma*

Research Institute of Powder Metallurgy, Central South University, Changsha 410083, China

* Corresponding authors:

E-mail: W. Liu, liuwensheng@csu.edu.cn;

Y. Ma, zhuzipm@csu.edu.cn

Received: October 17, 2026; Revised: November 17, 2026; Accepted: November 18, 2026

©The Author(s) 2026

Just Accepted

清華大學出版社 Tsinghua University Press | SciOpen

Abstract

Tungsten–silicon nitride (W/Si_3N_4) composite ceramics were prepared by spark plasma sintering (SPS) at 1650–1800 °C with W contents of 0–20 vol%. The effects of processing on interfacial reactions, microstructure and properties were examined by X-ray diffraction, microscopy and property measurements. W_5Si_3 was detected in the specimens sintered at 1650 and 1800 °C, while its peaks were not resolved at 1700–1750 °C. A change in local nitrogen transport during densification is proposed as a possible explanation for this temperature dependence. In the WSN20 specimen sintered at 1750 °C, atomic-resolution TEM revealed a local W/Y_2O_3 contact. The two reported lattice spacings differed by approximately 1.29% in one dimension. This interfacial structure is considered alongside the measured mechanical properties and thermal conductivity. The observations identify a temperature-dependent phase response and an oxide-derived metal/ceramic interface for further investigation; the effects of local nitrogen pressure and interfacial bonding on bulk properties remain to be established.

Keywords: silicon nitride; tungsten; spark plasma sintering; interfacial reactions; mechanical properties; thermal conductivity

1 Introduction

The strong covalent bonding and limited atomic self-diffusivity of silicon nitride (Si_3N_4) make it difficult to densify. Its relatively low fracture toughness and electrical conductivity also limit applications that require both damage tolerance and electrical conduction [1–3].

A second phase can improve the toughness and strength of ceramics. Metal particles, including Cu, Fe, Mo, Al, Ag, Ni and W, have been used to toughen ceramics and glasses [4–13]. Tungsten has a thermal expansion coefficient of 4.6×10^{-6} K^{-1} and

Just Accepted

an elastic modulus of 411 GPa. Its thermal compatibility with Si_3N_4 may limit residual stresses, while the interfaces introduced by W particles may alter crack initiation and propagation. Tungsten is also a refractory metal whose fracture behaviour changes with temperature; a brittle-to-ductile transition above 300 °C has been reported [14]. Combining W with Si_3N_4 may therefore offer a route to metal–ceramic composites that combine mechanical, thermal and electrical properties with the high-temperature and wear resistance of the ceramic.

Previous studies have examined the processing and toughening of Si_3N_4-based ceramics [15–21], as well as graphene additions for biomedical applications [22,23]. Metallic W is another candidate for toughening Si_3N_4. In gas-pressure-sintered W/Si_3N_4 composites, Yang et al. [24] reported relative densities above 97% for W contents below 5 wt%. At 5 wt% W, the flexural strength, Vickers hardness and fracture toughness were approximately 670 MPa, 16.4 GPa and 8.0 $MPa \cdot m^{1/2}$, respectively, representing increases of approximately 38%, 13% and 44% over W-free Si_3N_4. Crack deflection and branching near W particles were associated with this toughening response.

At W contents of 10–20 vol% or higher, contacts among W particles may contribute to electrical, dielectric or electromagnetic responses. Gas-pressure sintering has been used to prepare Si_3N_4-based metamaterials [25]. In that work, a nitrogen pressure of 10 MPa and a flowing nitrogen atmosphere were used to limit reactions and remove part of the oxidized tungsten, producing dense composites with no appreciable interfacial reaction layer.

W and Si_3N_4 can react at high temperature to form the brittle silicide W_5Si_3, which may degrade composite properties. Limiting this reaction is therefore a processing concern. Because the reaction can be thermodynamically favourable over the sintering

Just Accepted

range, its extent may depend on the kinetics and local nitrogen transport conditions as the compact densifies.

Spark plasma sintering (SPS) applies pulsed direct current and pressure, allowing high heating rates and short sintering times. SPS may therefore limit interfacial reaction while promoting densification of W–Si_3N_4 composites.

This work examines the effects of sintering conditions and W content on the phases, interfacial structure and properties of SPS-prepared W/Si_3N_4 composites. The analysis addresses two related questions: why W_5Si_3 diffraction peaks are not resolved within a temperature interval, and what local interface forms between W and the additive-derived oxide phase. FactSage calculations are considered alongside the XRD results, and TEM is used to examine a W/Y_2O_3 contact. The proposed roles of nitrogen transport and the interface in the measured properties require further verification.

2 Materials and methods

2.1 Starting materials

The α-Si_3N_4 powder (Ube Industries, Ltd., Japan) had an average particle size of 1.3 μm, an α-phase content of 95 wt%, a nitrogen content of 39.1 wt% and an oxygen content of 1.2 wt%. Yttria (Y_2O_3, 99.99%, 4 vol%) and alumina (Al_2O_3, 99.9%, 2 vol%) were added as sintering aids. Metallic W powder (99.9%, Zhangyuan Co., China) was added at 0–20 vol%.

2.2 Preparation of W/Si_3N_4 composites

Si_3N_4, the sintering aids and the designated amounts of W powder were weighed and mixed. Zirconia balls were added at a ball-to-powder mass ratio of 1:2.

The powders were mixed by resonant acoustic mixing (RAM). A mechanical resonance system generates low-frequency acoustic vibrations of approximately 60 Hz,

Just Accepted

with accelerations of up to 100 g. Under resonance, bulk motion and microscopic acoustic flow provide blade-free, non-contact mixing. The method is suitable for powders with a large density difference, such as W and Si_3N_4.

The vibration acceleration was set to 80 g and the equipment frequency to 60 ± 5 Hz. Three mixing cycles of 2 min each were performed.

The mixed powder was loaded into graphite dies whose inner walls were coated with hexagonal boron nitride (h-BN) as a diffusion barrier. Graphite foils were placed between the punches and powder to prevent adhesion. The composites were sintered by SPS under high-purity nitrogen at an applied pressure of 50 MPa using the specified sintering schedules. The specimens were then cooled to room temperature in the furnace. Table 1 lists the sample designations and nominal compositions.

Table 1. Sample designations and nominal compositions

Serial number	Y_2O_3（vol%）	Al_2O_3（vol%）	W（vol%）	Si_3N_4（vol%）
WSN0	4	2	0	balance
WSN5	4	2	5	balance
WSN10	4	2	10	balance
WSN15	4	2	15	balance
WSN20	4	2	20	balance

Just Accepted

2.3 Characterization

Phases were identified by X-ray diffraction (Ultima IV, Japan) using Cu Kα radiation over 2θ = 10–90°, a scan rate of 10° min^{-1} and a step size of 0.02°.

Bulk density was measured by the Archimedes method. Vickers hardness was measured using a microhardness tester (2100B, Wilson-Wolpert, Instron, USA).

Hardness and fracture toughness were derived from the indentation morphology; the latter is described here as an indentation-derived estimate.

Cross-sectional and polished-surface morphologies of the powders and sintered specimens were examined by scanning electron microscopy (SEM, EVO MA10, Germany) in secondary-electron and backscattered-electron modes. Elemental and phase compositions were analyzed using the attached energy-dispersive X-ray spectroscopy (EDS) and electron backscatter diffraction (EBSD) systems. The grain size of the metallic particles was examined by electron channelling contrast (ECC) in backscattered-electron mode after carbon coating. Selected-area electron diffraction (SAED) was performed using a JEOL JEM-2100UH transmission electron microscope operated at 200 kV to determine lattice parameters and orientation relationships. Bright-field and dark-field imaging were used to characterize the morphology, distribution and composition of secondary phases.

Thermal diffusivity was measured using a laser flash analyzer (LFA 467, Germany) at 300 °C under flowing nitrogen (50 mL min^{-1}). The reported specimen dimensions were 3 × 3 × 10 mm. The surfaces were polished and graphite-coated before measurement. Thermal conductivity was calculated from the measured diffusivity. Each measurement was repeated three times, and the mean was reported.

3 Results and discussion

Just Accepted

3.1 Phase analysis

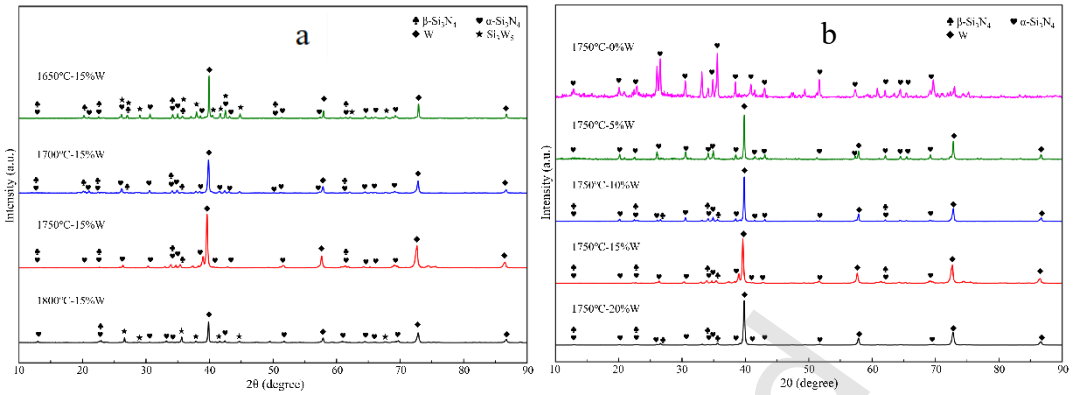


Figure 1. XRD patterns of SPS-prepared WSN composites:
(a) WSN15 at different temperatures; (b) composites with different W contents at 1750 °C.

Figure 1(a) shows the XRD patterns of W/Si_3N_4 composites sintered at different temperatures. In the 1650 °C specimen, peaks assigned to W_5Si_3 appear in addition to those of α-Si_3N_4 and W. These peaks are consistent with a reaction involving W and Si_3N_4 during SPS. Dissolution of Si_3N_4 at temperatures above 1400 °C and reaction of W with dissolved Si, accompanied by N_2 release, are possible steps in silicide formation.

At 1700 and 1750 °C, the peaks assigned to W_5Si_3 are no longer clearly resolved. Shimoo et al. [26] observed W_5Si_3 and WSi_2 at relatively low nitrogen partial pressures and reported further conversion of W_5Si_3 to WSi_2. Their results show that silicide formation depends on temperature, time and nitrogen partial pressure.

FactSage was used to analyze the W/Si_3N_4 reaction as a function of temperature and nitrogen partial pressure. Equilib calculations were also used to examine the effect of overall composition on the stable silicide phase. At approximately 1 atm N_2, the calculated Gibbs energy change for W_5Si_3 formation from W and Si_3N_4 ranges from −82.15 to −130.83 kJ mol^{-1} between 1650 and 1800 °C. The negative values indicate a

Just Accepted

thermodynamic driving force for formation over this range. W_5Si_3 was detected at 1650 and 1800 °C, whereas its peaks were not resolved at 1700 and 1750 °C. This difference does not necessarily contradict the equilibrium calculations: during SPS, reaction and densification occur together, and changes in pore structure can alter gas transport and the local nitrogen chemical potential. One possible explanation is that densification changes the local nitrogen environment at the interface. At 1800 °C, further liquid formation and Si_3N_4 decomposition ($Si_3N_4 \rightarrow 3Si + 2N_2$) may generate gas and change the pore network, potentially restoring conditions favourable for silicidation. These proposed transport and pressure changes were not measured directly.

Shimoo et al. [26] reported N_2 release during reaction at the W/Si_3N_4 interface and its possible escape through intergranular pores. At 1650 °C, interconnected open pores could allow N_2 to escape and maintain a relatively low local partial pressure. At 1700–1750 °C, densification may reduce open porosity and connectivity, restricting nitrogen transport and increasing the local N_2 chemical potential. Such accumulation could weaken the driving force for further silicidation. This interpretation is consistent with the calculated reaction tendency and reports of rapid Si_3N_4 densification [27–29], but direct measurements of pore connectivity and local gas pressure are needed to test it. Densification and reaction can also proceed on different time scales: closure of transport paths during the SPS hold may limit further reaction before equilibrium is reached.

The W peak intensity increases with W content. The relative intensity of β-Si_3N_4 peaks also changes with temperature, consistent with promotion of the α→β

Just Accepted

transformation at higher temperatures. Quantitative phase analysis would be needed to determine the transformed fraction.

Figure 1(b) compares the XRD patterns of composites containing 0–20% W at 1750 °C/50 MPa/10 min. No W_5Si_3 peak is clearly resolved in these patterns. This observation is consistent with a limited amount of detectable crystalline silicide, but it does not rule out reaction below the XRD detection limit. Restricted nitrogen escape during rapid densification is a possible explanation. Residual α-Si_3N_4 is also detected; a high heating rate, usually above 100 °C min^{-1}, and a short hold may limit the time available for transformation.

Just Accepted

3.2 Density and relative density

The density and relative density of the SPS-prepared W/Si_3N_4 composites vary with sintering temperature and W content. Temperature can affect the amount and mobility of the liquid phase, whereas W content can influence powder packing and liquid-phase composition. Particle rearrangement and dissolution–reprecipitation are inhibited when the liquid fraction is insufficient or its viscosity is high [29]. The density response may therefore reflect competition among liquid-assisted rearrangement, packing constraints and changes in the thermal and chemical environment.

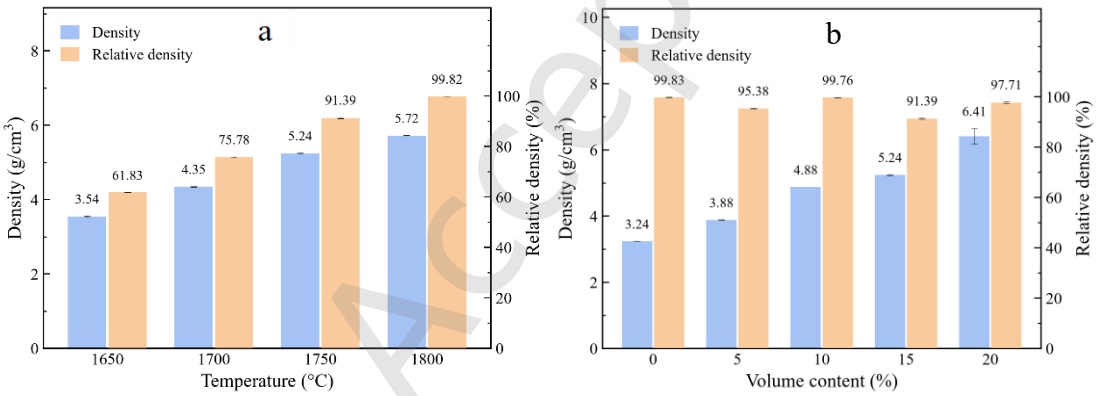


Figure 2. Bulk and relative densities of WSN composites:
(a) WSN15 at different temperatures; (b) composites with different W contents at 1750 °C.

Figure 2(a) shows that the density of WSN15 increases from 3.54 g cm^{-3} at 1650 °C to 5.72 g cm^{-3} at 1800 °C; the reported relative density at 1800 °C reaches 99.82%. Increased liquid formation, lower viscosity and improved wetting in the Y_2O_3–Al_2O_3 system may assist particle rearrangement and dissolution–reprecipitation. Higher diffusion rates of Si and N may also contribute. Above 1800 °C, Si_3N_4 decomposition

Just Accepted

($Si_3N_4 \rightarrow 3Si + 2N_2$) can impair properties. Considering densification and material stability, 1750 °C was selected for the W-content study.

In Figure 2(b), the relative density of WSN0 at 1750 °C/50 MPa/10 min is 99.83%. The reported values for WSN5 and WSN10 are 95.38% and 99.76%, respectively. Moderate W additions may affect particle rearrangement under pressure, liquid-phase composition and local temperature distribution. At 15% W, the relative density falls to 91.39%. Possible reasons include changes in powder packing, restricted liquid migration and particle contacts that inhibit matrix shrinkage. Wang et al. [30] also reported composition-dependent densification and microstructure in W-containing Si_3N_4. At 20% W, the relative density increases to 97.71%. A higher W content may promote particle contacts and alter liquid distribution, although a continuous network or a percolation threshold cannot be established from the density measurements alone.

Diffusion bonding between neighbouring W particles may affect the shrinkage of the compact, while changes in liquid flow may influence pore filling. These mechanisms could contribute to the composition-dependent density response, but the present measurements do not isolate their individual effects.

Just Accepted

3.3 Hardness and indentation-derived fracture toughness

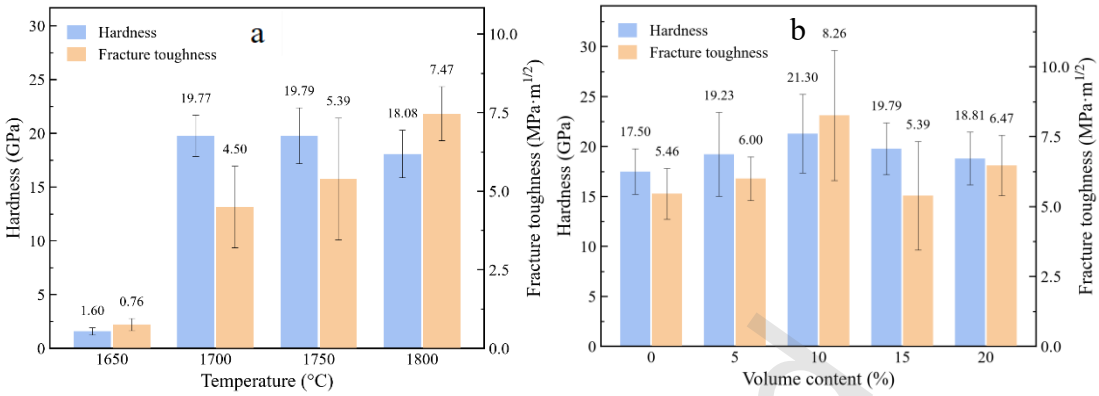


Figure 3. Hardness and indentation-derived fracture toughness of WSN composites: (a) WSN15 at different temperatures; (b) composites with different W contents at 1750 °C.

Figure 3 compares the hardness and indentation-derived fracture toughness of composites prepared under different conditions. Both properties vary with temperature and W content. Density, grain size, W distribution and interfacial bonding may all affect the response. Hardness reflects resistance to local deformation, while indentation-derived toughness is influenced by crack paths and energy-dissipation mechanisms such as deflection, bridging and pull-out.

For WSN15 sintered at 1650 °C, the hardness is 1.60 GPa and the indentation-derived fracture toughness is 0.76 MPa·m$^{1/2}$. The low values are consistent with insufficient densification and residual pores, which can concentrate stresses and facilitate crack propagation. Increasing temperature promotes liquid-assisted rearrangement and dissolution–precipitation. The reported hardness reaches 19.79 GPa at 1750 °C. At 1800 °C, the reported hardness and toughness are 18.08 GPa and 7.47 MPa·m$^{1/2}$, respectively. The change in hardness may reflect competing effects of densification and W-particle coarsening or agglomeration. The 1650 °C specimen has substantially lower relative density than the specimen sintered at 1750 °C, so porosity may be a dominant contributor to its low mechanical properties.

Just Accepted

In the 1700–1800 °C range, the hardness and indentation-derived toughness of most specimens increase markedly. The WSN10 specimen reaches 21.30 GPa and 8.26 MPa·m$^{1/2}$, respectively; related Si_3N_4 studies provide a context for comparison [30,31]. Possible contributors include densification, crack deflection or pinning by W particles, and bridging or pull-out of elongated β-Si_3N_4 grains. Higher temperature may also promote the α→β transformation. The hardness maximum reported for the WSN15 temperature series, 19.79 GPa at 1750 °C, and the WSN10 combination of 21.30 GPa and 8.26 MPa·m$^{1/2}$ refer to different specimens. Composition and temperature should therefore be considered together when comparing their properties.

Becher et al. [31] showed that the size and distribution of elongated β-Si_3N_4 grains affect fracture toughness through crack bridging, pull-out and deflection. Excessive grain growth may reduce strength, while local stress fields around coarse grains may promote microcracking. In the present composites, improved densification and interactions between cracks and W particles or interfaces are possible contributors to toughness. Inhomogeneous particle distribution, incomplete sintering or excessive grain growth may weaken these effects. Their individual contributions were not quantified.

3.4 Thermal conductivity

Just Accepted

Thermal diffusivity was measured by laser flash analysis, and thermal conductivity was calculated from the measurements. In Si_3N_4, heat transport depends on grain boundaries, lattice oxygen, grain connectivity and the structure of boundary phases [32–36]. Larger grains and fewer lattice defects can reduce phonon scattering, whereas amorphous boundary phases can increase it. Metallic W has a thermal conductivity of approximately 173 W m^{-1} K^{-1} and may contribute to heat transport in the composite.

Figure 4. Thermal conductivity and thermal diffusivity of WSN composites: (a) WSN15 at different temperatures; (b) composites with different W contents at 1750 °C.

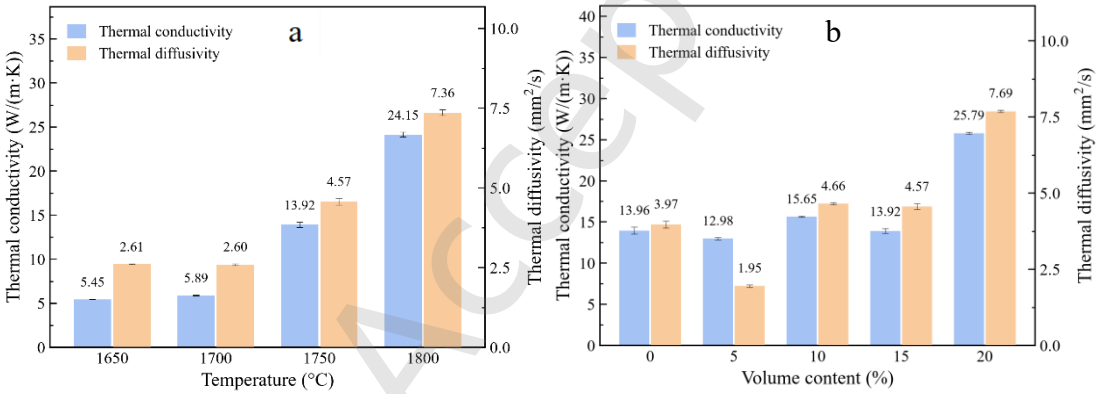


Figure 4 shows that thermal transport depends on W content as well as densification, particle distribution and interfaces. For WSN15 prepared at 1650 °C with a 10 min hold, the thermal conductivity and diffusivity are 5.45 W m^{-1} K^{-1} and 2.61 mm^2 s^{-1}, respectively. These low values are consistent with the low density of the specimen. Pores reduce the effective heat-transfer area and may increase scattering; grain-boundary phases and metal/ceramic contacts may also affect transport [37]. At 1750 °C, the reported conductivity decreases from 13.96 W m^{-1} K^{-1} for WSN0 to 12.98 W m^{-1} K^{-1} for WSN5 despite the high conductivity of W. Interfacial resistance and particle distribution are possible contributors, but conductivity alone does not establish a percolation threshold or a continuous W network.

Just Accepted

In the 1750 °C series, the conductivities of the 0%, 5% and 10% W specimens are 13.96, 12.98 and 15.65 W m^{-1} K^{-1}, respectively. For WSN20, the reported thermal conductivity and diffusivity are 25.79 W m^{-1} K^{-1} and 7.69 mm^2 s^{-1}, and its relative density is 97.71%. Lower porosity and W-assisted heat-transfer paths may contribute to the higher conductivity, but the connectivity and interfacial resistance were not measured directly.

3.5 Local interfacial structure of WSN20 at 1750 °C

Figure 5 shows the interface examined in the composite containing 20% W and sintered at 1750 °C. In Figure 5(a), W-rich regions occur as particles in the Si_3N_4 matrix. Y, Al and O are concentrated in grain-boundary regions adjacent to the particles, consistent with an additive-derived boundary phase. The close contact between W and Y–O-containing material provides an opportunity to examine a local W/oxide interface. The observed crystalline region may differ from amorphous boundary films, but a single local image does not establish the distribution or properties of all interfaces.

Figure 5(b) shows atomic-scale images from both sides of the interface. The FFT pattern of region 1 was indexed to body-centred cubic W along the [001] zone axis, with a d-spacing of $(\bar{1}10)$ of approximately 0.2247 nm. Region 2 was indexed to Y_2O_3 along the $[\bar{3}75]$ zone axis, with a d-spacing of approximately 0.2276 nm for the (233) plane. The lattice fringes are well defined on both sides. The two-phase FFT pattern in Figure 5(c) contains spots assigned to W and Y_2O_3, with the following local orientation relationships:

$$W[001] \parallel Y_2O_3[\bar{3}75]$$
$$W(\bar{1}10) \parallel Y_2O_3(233)$$

The measured spacings of the assigned parallel planes differ slightly.

The relative difference between the measured spacings was calculated as follows:

Just Accepted

$$f = \frac{|\, d_2 - d_1 \,|}{d_1} \times 100\%$$

The calculated relative difference between the two measured spacings is approximately 1.29% in one dimension. This value suggests a close spacing match for the assigned planes at the observed interface. It does not by itself establish a coherent interface, the absence of misfit dislocations, interfacial strength or a two-dimensional misfit. The proposed elastic accommodation over an observed width of 1–2 nm requires further verification.

In Figure 5(d), W and Y_2O_3 are in contact within the observed region, with no obvious void or continuous thick amorphous layer resolved near the interface. Lattice fringes are visible on both sides. Figure 5(e) shows Si and N mainly in the Si_3N_4 grains and Y, Al and O preferentially in grain-boundary regions. These observations are consistent with a locally crystallized boundary phase adjacent to W after sintering at 1750 °C.

The W/Y_2O_3 contact is an example of an interface between W and an oxide derived from a Si_3N_4 sintering aid. Its formation during densification suggests a possible route to interfacial design without a separate oxide-introduction step. The observed local contact does not establish a continuously distributed interfacial network, a uniform thickness of 1–2 nm throughout the composite, or performance under extreme service conditions. Those broader features would require further characterization.

In WSN20 sintered at 1750 °C, the observed W phase retains a body-centred cubic structure and contacts locally crystallized Y_2O_3 with the reported orientation relationship. Such a contact may affect load transfer and thermal transport, but its

Just Accepted

contribution cannot be separated from density, particle distribution and other interfaces. The specimen reaches a reported thermal conductivity of 25.79 W m^{-1} K^{-1}. Its hardness is lower than that of WSN15 in Figure 3(b); the higher fraction of relatively soft W may contribute to this difference.

W content and interfacial structure may affect hardness, fracture resistance and thermal conductivity differently. Further measurements of interfacial bonding, W connectivity and fracture paths are needed to establish these relationships and identify a composition range for optimization.

Just Accepted

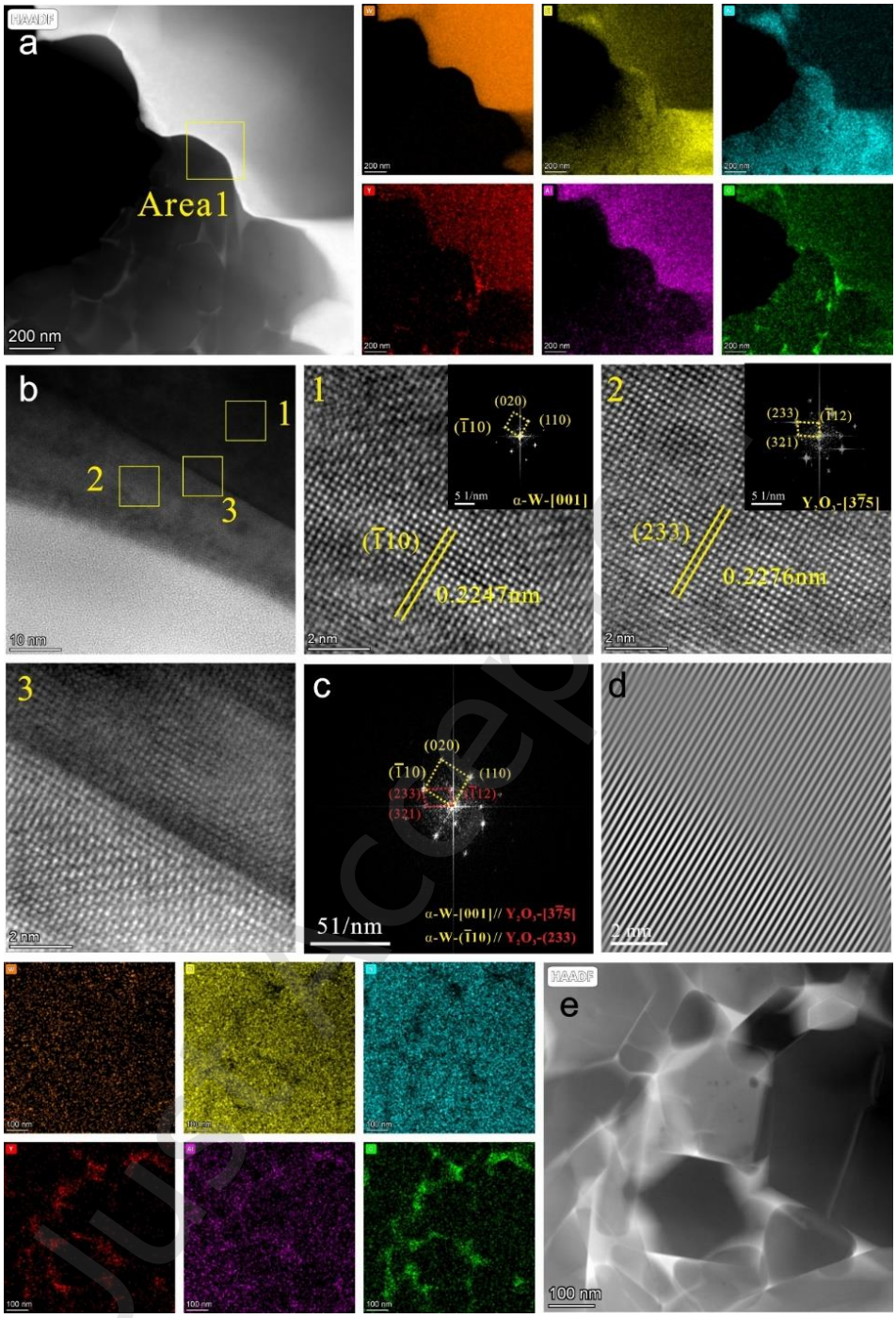


Figure 5. Local W/Y_2O_3 interface in WSN20 sintered at 1750 °C:

(a) HAADF-STEM image and elemental distribution around W particles; (b) HRTEM images of W and Y_2O_3; (c) two-phase FFT and orientation relationship; (d) processed lattice-fringe image; (e) elemental distribution in the Si_3N_4 matrix and grain-boundary phase.

4 Conclusions

In SPS-prepared W/Si_3N_4 composites, W_5Si_3 peaks were detected at 1650 and 1800 °C but were not clearly resolved at 1700–1750 °C. Changes in pore connectivity and local nitrogen partial pressure are proposed as possible contributors. The absence of resolved XRD peaks does not establish that no interfacial reaction occurred.

In the 1750 °C composition series, the highest reported hardness and indentation-derived toughness were obtained at 10 vol% W: 21.30 GPa and 8.26 MPa·$m^{1/2}$, respectively. The 20 vol% W composite had a reported thermal diffusivity of 7.69 mm^2 s^{-1} and a calculated thermal conductivity of 25.79 W m^{-1} K^{-1}, compared with 13.96 W m^{-1} K^{-1} for the W-free reference.

TEM observations of WSN20 sintered at 1750 °C show a local W/Y_2O_3 contact with the reported orientation relationship. The measured spacings differ by approximately 1.29% in one dimension. This observation provides a basis for studying additive-derived oxide interfaces in W/Si_3N_4 composites; further work is needed to establish their effect on fracture, thermal transport and electrical properties.

Acknowledgements

None.

Funding

No funding was received for conducting this study.

Just Accepted

Author contributions

Yu Zhou: Writing – original draft, Investigation, Formal analysis, Data curation, Writing – review & editing. Wensheng Liu: Supervision. Yunzhu Ma: Investigation.

Availability of data and materials

The data supporting the findings of this study are available from the corresponding authors upon reasonable request.

Competing interests

The authors declare that they have no competing interests relevant to the content of this article.

Use of AI-assisted technologies

OpenAI Codex was used to assist with English-language editing and manuscript formatting. The authors retain responsibility for the content of the manuscript.

References

[1] Heimann RB. Silicon Nitride Ceramics: Structure, Synthesis, Properties, and Biomedical Applications. Materials 2023, 16: 5142. https://doi.org/10.3390/ma16145142.

[2] Shimizu T, Takama KI, Enokishima H, et al. Silicon Nitride Turbocharger Rotor for High Performance Automotive Engines. SAE Technical Paper 900656, 1990. https://doi.org/10.4271/900656.

[3] Akande IG, Kazeem RA, Oluwole OO, et al. Production and characterization of low-density silicon nitride reinforced zinc nanocomposite coatings on mild steel for applications in marine and automotive industries. Heliyon 2024, 10: e36000. https://doi.org/10.1016/j.heliyon.2024.e36000.

Just Accepted

[4] Huang ZH, Yang JZ, Liu YG, et al. Novel Sialon-Based Ceramics Toughened by Ferro-Molybdenum Alloy. J Am Ceram Soc 2012, 95: 859–861. https://doi.org/10.1111/j.1551-2916.2011.05051.x.

[5] Sun Q, Yang J, Yin B, et al. High toughness integrated with self-lubricity of Cu-doped Sialon ceramics at elevated temperature. J Eur Ceram Soc 2018, 38: 2708–2715. https://doi.org/10.1016/j.jeurceramsoc.2018.01.042.

[6] Tuan WH, Brook RJ. The toughening of alumina with nickel inclusions. J Eur Ceram Soc 1990, 6: 31–37. https://doi.org/10.1016/0955-2219(90)90032-b.

[7] Sbaizero O, Pezzotti G. Influence of residual and bridging stresses on the R-curve behavior of Mo- and FeAl-toughened alumina. J Eur Ceram Soc 2000, 20: 1145–1152. https://doi.org/10.1016/s0955-2219(99)00267-8.

[8] Sekino T, Niihara K. Microstructural characteristics and mechanical properties for Al_2O_3/metal nanocomposites. Nanostruct Mater 1995, 6: 663–666. https://doi.org/10.1016/0965-9773(95)00145-x.

[9] Rodriguez-Suarez T, Lopez-Esteban S, Bartolomé JF, et al. Mechanical properties of alumina-rich magnesium aluminate spinel/tungsten composites. J Eur Ceram Soc 2007, 27: 3339–3344. https://doi.org/10.1016/j.jeurceramsoc.2007.02.192.

[10] Lalande J, Scheppokat S, Janssen R, et al. Toughening of alumina/zirconia ceramic composites with silver particles. J Eur Ceram Soc 2002, 22: 2165–2171. https://doi.org/10.1016/s0955-2219(02)00031-6.

[11] Yang JZ, Huang ZH, Fang MH, et al. Preparation and mechanical properties of Fe/Mo–Sialon ceramic composites. Scr Mater 2009, 61: 632–635. https://doi.org/10.1016/j.scriptamat.2009.05.042.

Just Accepted

[12] Li Y, Yu H, Jin H, et al. Effects of FeMo alloy on nitridation and mechanical properties of reaction bonded β-Sialon/FeMo ceramic composites. J Alloys Compd 2014, 616: 639–645. https://doi.org/10.1016/j.jallcom.2014.07.176.

[13] Lucchini E, Lo Casto S, Sbaizero O. The performance of molybdenum toughened alumina cutting tools in turning a particulate metal matrix composite. Mater Sci Eng A 2003, 357: 369–375. https://doi.org/10.1016/s0921-5093(03)00227-2.

[14] Shen T, Dai Y, Lee Y. Microstructure and tensile properties of tungsten at elevated temperatures. J Nucl Mater 2016, 468: 348–354. https://doi.org/10.1016/j.jnucmat.2015.09.057.

[15] Munir ZA, Anselmi-Tamburini U, Ohyanagi M. The effect of electric field and pressure on the synthesis and consolidation of materials: A review of the spark plasma sintering method. J Mater Sci 2006, 41: 763 – 777. https://doi.org/10.1007/s10853-006-6555-2.

[16] Chen F, Shen Q, Yan F, et al. Spark plasma sintering of α-Si_3N_4 ceramics with MgO–$AlPO_4$ as sintering additives. Mater Chem Phys 2008, 107: 67–71. https://doi.org/10.1016/j.matchemphys.2007.06.042.

[17] Peng GH, Liang M, Liang ZH, et al. Spark Plasma Sintered Silicon Nitride Ceramics with High Thermal Conductivity Using $MgSiN_2$ as Additives. J Am Ceram Soc 2009, 92: 2122–2124. https://doi.org/10.1111/j.1551-2916.2009.03139.x.

[18] Lee CH, Lu HH, Wang CA, et al. Effect of Heating Rate on Spark Plasma Sintering of a Nanosized β-Si_3N_4 -Based Powder. J Am Ceram Soc 2011, 94: 1182–1190. https://doi.org/10.1111/j.1551-2916.2010.04196.x.

Just Accepted

[19] Khajelakzay M, Bakhshi SR, Borhani GH, et al. Synthesis and spark plasma sintering of the α-Si_3N_4 nanopowder. Ceram Int 2016, 42: 14867–14872. https://doi.org/10.1016/j.ceramint.2016.06.123.

[20] Cao L, Wang Z, Yin Z, et al. Investigation on mechanical properties and microstructure of silicon nitride ceramics fabricated by spark plasma sintering. Mater Sci Eng A 2018, 731: 595–602. https://doi.org/10.1016/j.msea.2018.06.093.

[21] Liu S, Pan Y, Feng B, et al. Toughening of silicon nitride ceramics through stress-induced phase transformation. J Adv Ceram 2025, 14: 9221125. https://doi.org/10.26599/JAC.2025.9221125.

[22] Zhan Z, Deng B, Chen Y, et al. Synergistic improvement of the mechanical and biological performance of Si_3N_4 by incorporating nanostructured graphene. J Adv Ceram 2025, 14: 9221026. https://doi.org/10.26599/JAC.2024.9221026.

[23] Zhan Z, Chen YR, Ainuer A, et al. Fundamentals and application research progress of silicon nitride bioceramic materials. Advanced Ceramics 2025, 46: 542–568. https://doi.org/10.16253/j.cnki.37-1226/tq.2025.06.003.

[24] Yang C, Zhou CL, Wang Q, et al. Effect and toughening mechanism of tungsten addition on mechanical properties of Si_3N_4 ceramics. Bulletin of the Chinese Ceramic Society 2023, 42: 287–293 (in Chinese).

[25] Wang L, Liu X, Qi Q, et al. A new type of dense silicon nitride-based metamaterial. J Adv Ceram 2025, 14: 9221037. https://doi.org/10.26599/jac.2025.9221037.

[26] Shimoo T, Sandjaja A, Adachi S, Okamura K. Kinetics of reaction at interface of Si_3N_4/W joint. J Ceram Soc Jpn 1995, 103: 108–112.

Just Accepted

[27] Wei ZL, Liu SY, Liu DG, et al. Fabrication and properties of symmetrical W/Si_3N_4/W functionally graded materials by spark plasma sintering. J Alloys Compd 2022, 896: 163077. https://doi.org/10.1016/j.jallcom.2021.163077.

[28] Shen Z, Nygren M. Kinetic aspects of superfast consolidation of silicon nitride based ceramics by spark plasma sintering. J Mater Chem 2001, 11: 204–207. https://doi.org/10.1039/B003200J.

[29] Hotta M, Hojo J. Nanostructure control of liquid-phase sintered Si_3N_4 ceramics by spark plasma sintering. J Ceram Soc Jpn 2009, 117: 1302–1305. https://doi.org/10.2109/jcersj2.117.1302.

[30] Wang L, Qi Q, Zhang H, et al. High tough W-added silicon nitride ceramics. Ceram Int 2019, 45: 19055–19059. https://doi.org/10.1016/j.ceramint.2019.06.148.

[31] Becher PF, Sun EY, Plucknett KP, et al. Microstructural Design of Silicon Nitride with Improved Fracture Toughness: I, Effects of Grain Shape and Size. J Am Ceram Soc 1998, 81: 2821–2830. https://doi.org/10.1111/j.1151-2916.1998.tb02702.x.

[32] Li Y, Kim HN, Wu H, et al. Microstructure and thermal conductivity of gas-pressure-sintered Si_3N_4 ceramic: the effects of Y_2O_3 additive content. J Eur Ceram Soc 2021, 41: 274–283. https://doi.org/10.1016/j.jeurceramsoc.2020.08.035.

[33] Zhou Y, Hyuga H, Kusano D, et al. Development of high-thermal-conductivity silicon nitride ceramics. J Asian Ceram Soc 2015, 3: 221–229. https://doi.org/10.1016/j.jascer.2015.03.003.

[34] Golla BR, Ko JW, Kim JM, et al. Effect of particle size and oxygen content of Si on processing, microstructure and thermal conductivity of sintered reaction

Just Accepted

bonded Si_3N_4. J Alloys Compd 2014, 595: 60–66. https://doi.org/10.1016/j.jallcom.2014.01.131.

[35] Li Y, Kim HN, Wu H, et al. Improved thermal conductivity of sintered reaction-bonded silicon nitride using a BN/graphite powder bed. J Eur Ceram Soc 2017, 37: 4483–4490. https://doi.org/10.1016/j.jeurceramsoc.2017.05.045.

[36] Kim JM, Ko SI, Kim HN, et al. Effects of microstructure and intergranular glassy phases on thermal conductivity of silicon nitride. Ceram Int 2017, 43: 5441–5449. https://doi.org/10.1016/j.ceramint.2017.01.037.

[37] Wang L, Qi Q, Zheng J, et al. A novel thermally matched conductive phase of silicon nitride ceramics. J Phys Chem Solids 2023, 179: 111379. https://doi.org/10.1016/j.jpcs.2023.111379.

Just Accepted